

Demonstration of Simultaneous Localization and Imaging With Multirotor-Borne MiniSAR

Yixiang Luomei , *Student Member, IEEE*, Feng Xu , *Senior Member, IEEE*, Feng Wang , *Member, IEEE*, and Yongwei Dong, *Member, IEEE*

Abstract—This article extends the segmental aperture imaging (SAI) algorithm, which tackles the challenges of synthetic aperture radar (SAR) imaging of miniaturized synthetic aperture radar (MiniSAR) onboard multirotor unmanned aerial vehicle (UAV). The SAI algorithm is developed based on an accurate phase error model of both translational and rotational motion of UAV. It does not require auxiliary positioning data such as global positioning system/inertial navigation system. We further extend it to simultaneously estimate and reconstruct the three-dimensional (3-D) trajectory of UAV from parameters derived from SAI motion compensation. Thus, it in fact accomplishes the simultaneous location and imaging (SLAI) using UAV-borne radar. It is first validated and evaluated via raw signal simulation using realistic trajectory data. For experiment purpose, a multirotor-borne MiniSAR system FUSAR-Ku is developed. Experimental results show that the proposed algorithm can achieve decimeter-resolution imaging performance as measured by various metrics, while simultaneously accomplishing centimeter-to-decimeter 3-D self-positioning capability. It is a first demonstration of SLAI mode with a multirotor-borne MiniSAR.

Index Terms—Miniaturized synthetic aperture radar (MiniSAR), motion compensation, multirotor unmanned aerial vehicle (UAV), segmental aperture imaging (SAI), simultaneous location and imaging (SLAI).

I. INTRODUCTION

MINIATURIZED synthetic aperture radar (MiniSAR) has the characteristics of small size, light weight, and low power consumption (SWaP), and is generally equipped on small mobile platform, such as unmanned aerial vehicles (UAVs) [1]–[8]. The portable system setup and easy experimental preparation make it possible to acquire SAR images with multiple incident angles and multiple orbits more flexibly [9]. It is convenient for various applications such as local terrain mapping or target scattering measurement [10]. MiniSAR can also perform data fusion with spaceborne SAR and manned airborne SAR to form a multiheight, multidimensional, and multilevel remote sensing system. Various remote sensing systems have

reference clocks, so data fusion at the signal level is complex. The usual practice is to fuse the data at the pixel level. That is, after each sensor is imaged, the two-dimensional (2-D) imaging results are fused. We generally use the spatial correlation of the target to perform geometric registration, geocoding, and other operations on the image, and then perform stitching and fusion [11]. For small maneuvering platforms, not only high-resolution and high-precision imaging algorithms are required, but also high-sampling rate positioning information to better restore the motion features of the platform [12].

Due to the SWaP of the multirotor UAVs (multirotors) platform, and the rapid development of high-speed digital processing technology, MiniSAR systems mostly use FMCW technology to reduce the system ADC sampling rate and the cost of analog circuits [3], [4]. In 2004, Brigham-Young University Microwave Earth Remote Sensing developed a low-cost microASAR system with a center frequency of 5.56 GHz (C-band) and a bandwidth of 80 MHz [13]. The power is 16 W, and the weight of the main components of the whole system is about 2 kg. In order to pursue portability, the noise suppression ratio and channel isolation of the system are low, resulting in a low signal-to-noise ratio and strong speckle noise in the image. Its imaging algorithm adopts classic back projection algorithm, and uses high-precision (accuracy about one-tenth of a wavelength) global positioning system (GPS) data for motion compensation [14]. In the case of continuous waves, it does not consider the intrapulse modulation caused by platform movement, which causes the signal model violating the “stop-and-go” model assumption. In 2005, Delft University of Technology developed an X-band SAR system, named TuDelft, mounted on a fixed-wing UAV [15], which solved the problems of continuous intrapulse motion and frequency nonlinearity. Sandia Laboratory of the United States and the German European Aeronautic Defence and Space Company (EADS) have successively developed the Ka-band Mini-SAR and MiSAR [16], [17]. The quality of the system imaging results completely depends on the accuracy of the GNSS system [17]. Later, Germany’s MIRANDA35 system [17] and SUMATRA system [18], China’s NUA-MiniSAR [9], IECAS-SAR [8] are the first to use auto-focusing algorithm, such as map-drift [19], phase gradient auto-focus [20], [21], and minimum entropy auto-focus [22], which does not rely on inertial navigation system (INS) for high-resolution imaging. These autofocusing algorithms have the disadvantages of only estimating the second-order error, requiring isolated feature points, and high computational complexity [23]–[25].

Manuscript received 28 June 2022; revised 4 July 2022; accepted 6 July 2022. Date of publication 14 July 2022; date of current version 18 August 2022. This work was supported by NSAF under Grant U2130202. (Corresponding author: Feng Xu.)

Yixiang Luomei, Feng Xu, and Feng Wang are with the Key Lab for Information Science of Electromagnetic Waves (MoE), Fudan University, Shanghai 200433, China (e-mail: 18110720072@fudan.edu.cn; fengxu@fudan.edu.cn; fengwang@fudan.edu.cn).

Yongwei Dong is with the Aerospace Information Research Institute, Chinese Academy of Sciences, Beijing 100190, China (e-mail: ywdong@mail.ie.ac.cn). Digital Object Identifier 10.1109/JSTARS.2022.3190940

However, most MiniSAR systems and algorithms are developed to work onboard stationary platforms such as fixed-wing UAVs, and often mounted with stabilizing technologies such as antenna servo systems. The challenges of multirotor-borne MiniSAR imaging can be summarized as unstable trajectories, unique maneuvering errors, inaccurate positioning, and orientation information, which are described in detail in [26]. To address these challenges, the segmental aperture imaging (SAI) algorithm is proposed [26]. The basic idea is to perform imaging segment by segment independently along the trajectory. For each stable segment, its accurate trajectory is estimated by fitting a polynomial phase history function. Segmental motion compensation is then performed to obtain focused segmental subimages which are then further stitched together to form the complete SAR image.

UAV MiniSAR has the characteristics of miniaturization, low test cost, and high freedom of laboratory parameters such as orbit and incidence angle. In order to give full play to its advantages, we need to obtain the position information of the platform at the same time in the imaging. If the MiniSAR finds a target of interest during the mission, it can interact with the UAV navigation system to adjust the flight trajectory in time for multiangle and multiorbit illumination. It provides a basis for the follow-up UAV intelligence and cluster work. Ultimately, we achieve two goals: 1) We use SLAI to provide alternative positioning approach in GPS-denied situation, to accomplish imaging without auxiliary positioning; and 2) the relative positioning of the SLAI with respect to the observed scene. Provide a technical approach for autonomous navigation and exploration for UAV.

Scholars from Delft University, The Netherlands, believe that the platform trajectory shows the periodic swing in coherent integration time [27], [28]. They use multibeam to illuminate the reference target on both sides of the trajectory. And then, they estimated the motion parameters of the platform after imaging, achieving an accuracy close to the resolution. Referring to this idea, under the condition of the motion trajectory closing to a straight line or a curve with a slight curvature, when imaging with single-channel data, the incident angle difference between segments is used to estimate the motion trajectory of the platform, making it possible to positioning and imaging simultaneously; moreover, after calculating the precise trajectory of each channel, we can correct the relative phase difference to achieve the effect of phase preservation.

In this article, the SAI algorithm is further extended for simultaneously location and imaging (SLAI), where it estimates and reconstructs the 3-D trajectory of the platform based on parameters derived from the motion compensation of SAI. An image correction scheme is also proposed, which is crucial for real data processing. A newly built FUSAR-Ku system onboard a multirotor platform is presented. The algorithm is applied to the system and demonstrates superior focusing and positioning performance to conventional methods. It demonstrated, for the first time, SLAI with a multirotor-borne radar.

The reminder of the article is organized as follows. Section II introduces the design and development of FUSAR-Ku system. Section III presents the algorithm extensions on SLAI, and image correction. In Section IV, a simulation using real radar

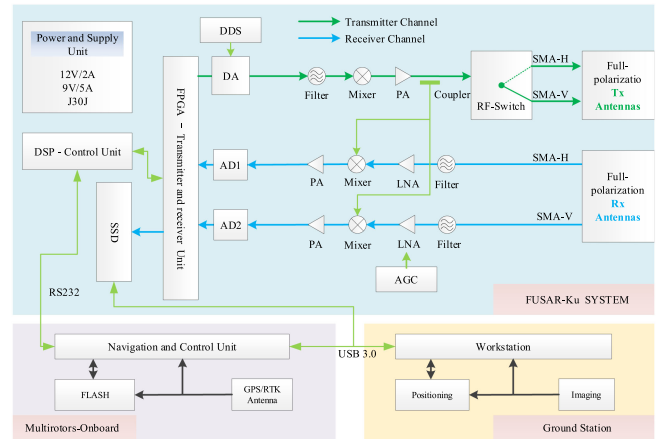


Fig. 1. Block diagram of FUSAR-Ku MiniSAR system, including control unit, transmitter and receiver unit, digital signal source unit, signal acquisition and processing unit, navigation and control unit, and power supply unit.

system parameters and motion trajectories are carried out to demonstrate the extended algorithm. Experimental results are shown in Section V. Section VI concludes the article.

II. FUSAR-KU SYSTEM

A multirotor-borne MiniSAR system named FUSAR-Ku is developed for experiment purpose. A block diagram of our system is shown in Fig. 1. The system consisting of control unit, transmitter and receiver unit, signal acquisition and processing unit, navigation and control unit, and power supply unit is mounted onboard a UAV platform equipped with a navigation device.

The control unit controls the overall timing of the system and synchronizes the time of each sensor in the system. The transmitter and receiver unit include transmitter and receiver channels, as shown in Fig. 1. The transmit channel contains a waveform generator, which generates a sawtooth wave signal with a bandwidth of 300 MHz. It is then multiplied and mixed with a 13 GHz local oscillator to obtain an FMCW with a center frequency of 15.2 GHz (Ku-band) and a max bandwidth of 1.2 GHz. Finally, it is radiated to the imaging area via the transmitting antennas (Tx antennas), followed by a power amplifier. System specifications are the transmitter power of 5 W, the antenna gain of 23 dB, and the system noise figure of 4 dB, while sweep time can be adjusted between 500 and 2000 μ s.

After the receiving antennas (Rx antennas) receive the echo signal, it is amplified by a low-noise amplifier and mixed with the reference signal by dechirp operation to obtain the beat signal. The ADC samples the beat signal and stores it in the solid-state disk (SSD). Simultaneously, the dechirp operation has reduced the sampling rate to 25 MHz. The ground workstation reads the raw data stored in the SSD through the USB3.0 interface and uses the SAI algorithm to perform high-resolution imaging on the ground [26].

The system includes two Tx antennas and two Rx antennas, which are H and V polarization modes, respectively. Four channels of fully polarized (HH, HV, VH, VV) raw data can

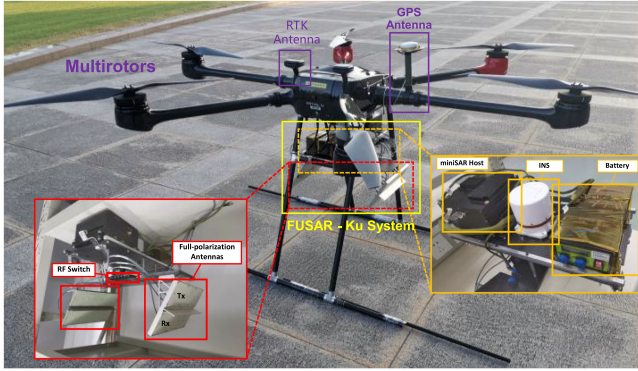


Fig. 2. Optical image of the FUSAR-Ku MiniSAR system and a multirotor platform.

be obtained in one flight. The radar system itself and it being mounted on a multirotor are pictured in Fig. 2. The antenna is installed perpendicular to the right side of its nose, and the antenna points to the right. The incident angle is 65° . The distance between the two antennas is 50 cm.

We have installed GPS, INS, and real-time kinematic (RTK) antennas on the multirotor for the navigation and control unit to fly according to the planned trajectory. The weight is 1.1 kg, and the positioning accuracy is 1.5–3 m. The digital signal processing (DSP) connects UAV navigation system with MiniSAR. The DSP reads the latitude, longitude, and altitude coordinates of the current platform, and controls MiniSAR to turn ON/OFF the transmitter and receiver at the desired position. Note that the GPS/INS measurements are later used for validation purpose only, but not used for imaging. It means that the radar system itself does not rely on the GPS/INS. Instead, the radar could be used simultaneously as a positioning system to replace GPS/INS if real-time imaging is implemented in future.

The control unit, transmitter and receiver unit, digital signal source unit, signal acquisition and processing unit, and navigation and control unit are all integrated into one box as shown in Fig. 2. And the power supply unit ensures the continuous operation of the system, which is provided by a 10 000 mA lithium battery. The system weighs about 6 kg.

III. ALGORITHM EXTENSIONS

A. Phase Estimation

A comprehensive signal model tailored for MiniSAR onboard multirotor platform is derived in [26], which described the relationship between the errors of the platform motion speed, attitude angle, and vibration frequency and the phase error of the target echo. The instantaneous phase is derived as follows:

$$\phi(\eta) = \phi_o(\eta) + \phi_e(\eta) - \phi_s(\eta) \quad (1)$$

where η means the azimuth sampling time and $\phi_o(\eta)$ represents the ideal phase without errors. It is approximated as a second-order polynomial of η , the first-order coefficient is related to the Doppler center, and the second-order coefficient is related to the Doppler frequency modulation slope.

$\phi_e(\eta)$ describes the phase error due to platform position and attitude errors

$$\phi_e(\eta) = -\frac{4\pi}{\lambda} (\Delta y \sin(\theta_{in} + \theta_e) + \Delta z \cos(\theta_{in} + \theta_e)) \quad (2)$$

where λ is the wavelength of the transmitted signal, θ_{in} is the incident angle of the system, and θ_e is the angle between the error vector and the line of sight (LoS). The error vector is the position error $(\Delta x, \Delta y, \Delta z)$ after the rotation of the attitude angle (roll angle, yaw angle, and pitch angle). $\Delta x, \Delta y,$ and Δz represent the error projections in the $X, Y,$ and Z directions, respectively, which are obtained from the system original position error and attitude angle error through rotation and translation transformation, and they have different values at each Doppler frequency sampling point.

$\phi_s(\eta)$ represents the phase error caused by high-frequency vibration

$$\phi_s(\eta) = \xi \sin(w_r \eta) \quad (3)$$

where w_r is the frequency of high-frequency vibration and ξ indicates the projection of the vibration magnitude A_r in the LoS

$$\xi = A_r (\sin \theta_e \cos(\theta_{s_e} + \theta_{y_e}) \sin(\theta_{r_e}) - \cos \theta_{r_e} \cos(\theta_{r_e})) \quad (4)$$

where $\theta_{s_e}, \theta_{y_e},$ and θ_{r_e} are obtained by projecting the position and attitude coupling errors on the XOY plane, the YOZ plane, and the XOZ plane, respectively.

The SAI algorithm [26] can be used to estimate the position and attitude of platform simultaneously while performing auto-focusing for imaging. Considering the instability of the motion of platform, we divide the echo signal into M segments along the azimuth dimension, and perform polynomial fitting on the phase segment by segment. Equations (1)–(4) establishes the relationship between the motion parameters and the instantaneous phase.

In segment $q, q = 1 \dots M,$ we extract the phase $\phi_q(\eta_q)$ from the raw data, and the fitted instantaneous phase $\hat{\phi}_q(\eta_q)$ can be expressed as follows:

$$\hat{\phi}_q(\eta_q) = \beta_q \eta_q^2 + \alpha_q \eta_q + \varphi_{0,q} \quad (5)$$

where η_q means the azimuth time of segment q, β_q and α_q are the coefficients of the second-order and first-order terms of the fitted phase, respectively, and $\varphi_{0,q}$ is a constant term caused by high-frequency vibration.

The estimated value of ξ for the q th segment is as follows:

$$\hat{\xi}_q = \left(\frac{8\pi K_r R_{s,q}^2}{c^2} - \varphi_{0,q} \right) \frac{\lambda}{4\pi} \quad (6)$$

where c is the speed of light, K_r means the frequency slope of transmitted signal, and $R_{s,q}$ is the reference range of segment $q,$ calculated from the shortest slant range and the squint angle.

By analyzing the high-frequency components of $\phi_q(\eta_q),$ we can estimate the phase error caused by high-frequency vibration $\hat{\phi}_{s,q}(\eta_q).$

According to (1), we can estimate the phase errors $\hat{\phi}_{e,q}(\eta_q)$ of segment q

$$\hat{\phi}_{e,q}(\eta_q) = \hat{\phi}_q(\eta_q) - \beta_q \eta_q^2 - \alpha_q \eta_q - \hat{\phi}_{s,q}(\eta_q). \quad (7)$$

After obtaining the phase errors of each order $\hat{\phi}_{e,q}(\eta_q)$, $\hat{\phi}_s(\eta_q)$, phase compensation is performed on the raw data after range compression, and finally the focused SAR image can be obtained by multiplying the matched filter.

B. Platform Positioning, Trajectory Reconstruction, and SLAI

We write the phase $\phi(\eta)$ in (5) as a Taylor expansion, and we obtain the relationship between the Doppler frequency slope $K_{a,q}$ and the Doppler center $f_{dc,q}$ in the q th segment and the coefficients of the first-order and second-order terms

$$K_{a,q} = \frac{\beta_q}{\pi} \quad (8)$$

$$f_{dc,q} = \frac{\alpha_q}{2\pi}. \quad (9)$$

The estimated value of β_q and α_q are in [26, Eqs. (17), (18)]. Substitute the estimated values of β_q and α_q into (7) and (8), and then add the second and first derivatives of the higher order phase $\hat{\phi}_{s,q}(\eta_q)$ to obtain the estimated values of the $K_{a,q}$ and the Doppler center $f_{dc,q}$

$$\hat{K}_{a,q} = -\frac{2\hat{v}_q^2 \cos^2 \theta'_{s,q}}{\lambda R_{s,q}} + \frac{d^2 \hat{\phi}_{s,q}(\eta_q)}{2\pi d\eta_q^2} \quad (10)$$

$$\hat{f}_{dc,q} = \frac{2\hat{v}_q \sin \theta'_{s,q}}{\lambda} + \frac{d\hat{\phi}_{s,q}(\eta_q)}{2\pi d\eta_q} \quad (11)$$

where $\frac{d(\cdot)}{d\eta_q}$ denotes the derivative with respect to η_q . The instantaneous velocity \hat{v}_q and squint angle $\theta'_{s,q}$ are calculated from the relationship between the estimated phase history $\hat{\phi}_q(\eta_q)$ and the Doppler parameters $K_{a,q}$ and $f_{dc,q}$, and details are in (22) in [26]. λ is the wavelength.

Assuming in segment q , we consider the trajectory of the multirotor to be linear, as shown in Fig. 3, the blue line. In the XYZ coordinate system of segment q , the linear trajectory coordinates are as follows:

$$\begin{bmatrix} X_q \text{ in } q \\ Y_q \text{ in } q \\ Z_q \text{ in } q \end{bmatrix} = \begin{bmatrix} \int \hat{v}_q \sin \theta'_{s,q} d\eta_q \\ \int \hat{v}_q \sin(\theta_{in} + \theta_e) d\eta_q + \int \hat{v}_q \cos \theta'_{s,q} d\eta_q \\ R_{s,q} \cos \theta'_{s,q} \cos \theta_{in} + \theta_e + \int \hat{v}_q \cos(\theta_{in} + \theta_e) d\eta_q \end{bmatrix}. \quad (12)$$

The track coordinates of the adjacent segment $q+1$ can also be written in the form of (12) in the $q+1$ coordinate system $[X_{q+1} \text{ in } q+1, Y_{q+1} \text{ in } q+1, Z_{q+1} \text{ in } q+1]^T$. As shown in Fig. 4, there is a rotation angle $(\theta_{x,q+1}, \theta_{y,q+1}, \theta_{z,q+1})$ in the coordinate system between two adjacent segments. Let us use the coordinate system of segment q as the reference coordinate system. Choose at least three points in the area where the two apertures intersect. The coordinates are $[Q_{1,q}, Q_{2,q}, Q_{3,q}]_{3 \times 3}$ in

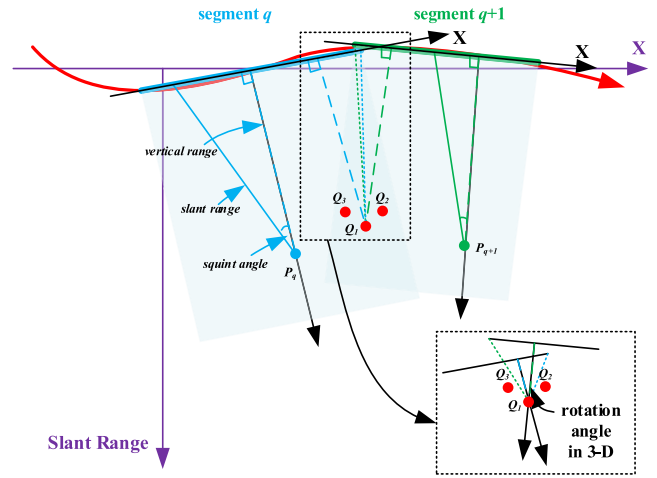


Fig. 3. Schematic diagram of trajectory estimation. The blue one is the segment q coordinate system, and the green one is the segment $q+1$ coordinate system. There is a rotation angle between the two coordinate systems. The blue point is the point of the complete aperture in the segment q . The point of the full aperture among the green points segment $q+1$. The red point is the point where the two apertures intersect, and it is the point of incomplete aperture in both segments.

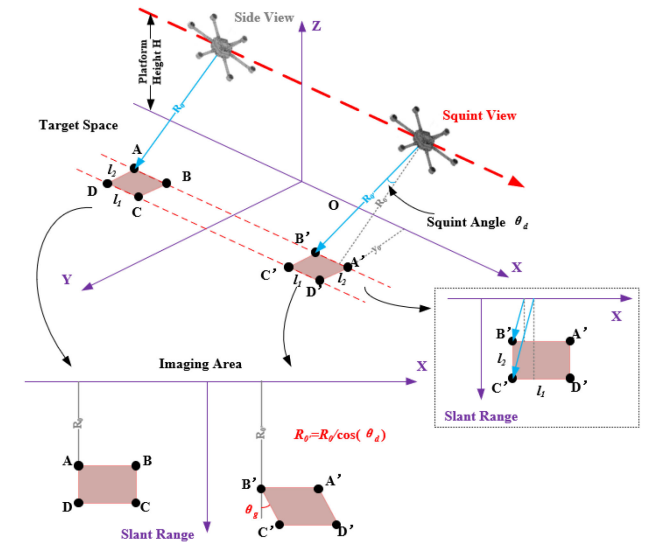


Fig. 4. MiniSAR detects four points $ABCD$ and $A'B'C'D'$ on the ground with side/squint view, respectively. $A'B'C'D'$ is symmetric with $ABCD$ about the Y -axis. In squint mode, the rectangle formed by the four points of $ABCD$ will become a parallelogram.

segment q , and the coordinates are $[Q_{1,q+1}, Q_{2,q+1}, Q_{3,q+1}]_{3 \times 3}$ in segment $q+1$.

According to the rotation matrix, the relationship between the two coordinates is as follows:

$$[Q_{1,q}, Q_{2,q}, Q_{3,q}]_{3 \times 3} = \begin{bmatrix} 1 & 0 & 0 \\ 0 & \cos \theta_{x,q+1} & -\sin \theta_{x,q+1} \\ 0 & \sin \theta_{x,q+1} & \cos \theta_{x,q+1} \end{bmatrix} \cdot \begin{bmatrix} \cos \theta_{y,q+1} & 0 & -\sin \theta_{y,q+1} \\ 0 & 1 & 0 \\ \sin \theta_{y,q+1} & 0 & \cos \theta_{y,q+1} \end{bmatrix}$$

$$\begin{aligned}
& \cdot \begin{bmatrix} \cos \theta_{z,q+1} & -\sin \theta_{z,q+1} & 0 \\ \sin \theta_{z,q+1} & \cos \theta_{z,q+1} & 0 \\ 0 & 0 & 1 \end{bmatrix} \\
& \cdot [\mathbf{Q}_{1,q+1}, \mathbf{Q}_{2,q+1}, \mathbf{Q}_{3,q+1}]_{3 \times 3} \\
& = \Upsilon \cdot [\mathbf{Q}_{1,q+1}, \mathbf{Q}_{2,q+1}, \mathbf{Q}_{3,q+1}]_{3 \times 3}. \quad (13)
\end{aligned}$$

Solving the rotation angle directly will increase the difficulty of the solution, so we choose three points to solve the rotation matrix Υ

$$\Upsilon = [\mathbf{Q}_{1,q}, \mathbf{Q}_{2,q}, \mathbf{Q}_{3,q}]_{3 \times 3} \cdot [\mathbf{Q}_{1,q+1}, \mathbf{Q}_{2,q+1}, \mathbf{Q}_{3,q+1}]_{3 \times 3}^{-1}. \quad (14)$$

Calculate the coordinates of the platform trajectory of segment $q+1$ in the q coordinate system

$$\begin{bmatrix} \mathbf{X}_{q+1 \text{ in } q} \\ \mathbf{Y}_{q+1 \text{ in } q} \\ \mathbf{Z}_{q+1 \text{ in } q} \end{bmatrix} = \Upsilon \cdot \begin{bmatrix} \mathbf{X}_{q+1 \text{ in } q+1} \\ \mathbf{Y}_{q+1 \text{ in } q+1} \\ \mathbf{Z}_{q+1 \text{ in } q+1} \end{bmatrix}. \quad (15)$$

The above operation is conducted section by section to unify all segment trajectory in the reference segment coordinate system.

Note that, in this part, the Y -axis in the coordinate system here represents the slant range, as shown in Fig. 3. It is the azimuth-slant range-altitude coordinate system. After that, we project the slant range to the ground range according to the imaging geometry, where the error caused by the roll angle will be introduced. If an absolute position of a group of Q points in the image can be obtained (such as the coordinate of the WGS-84 coordinate system), the absolute position of the estimated trajectory can then be estimated accordingly.

The proposed method has, in fact, established an SLAI algorithm for multirotor-borne radar for the first time. Based on this, more interesting topics could be studied in the future.

C. Image Correction

UAV has relatively poor wind resistance. Large fluctuations may appear in one section of the image, while other sections are very stable. At this time, it is not only the phase of the echo signal that is affected, but its amplitude may also be affected. According to the radar equation, if the system remains unchanged, and the RCS of target area observed by the radar system does not change significantly, the echo power is inversely proportional to the fourth power of the range. The image will be distorted by this received power relationship. Moreover, when stitching segments, there may be differences in amplitude for different segments. Thus, each segment image is corrected by multiplying a scale factor which is estimated by matching the brightness histograms of different segment images.

When a multirotor flies in a certain direction, its pitch angle will affect the beam center direction. Therefore, MiniSAR will change from side view to slightly squint view. As shown in Fig. 4, ABCD and A'B'C'D' are two identical rectangles with edges l_1 and l_2 , which are located on the XOY plane with distance y_0 to the X -axis, and the perpendicular slant range of the flight track is R_0 . For the squint view case, the rectangular target will become a

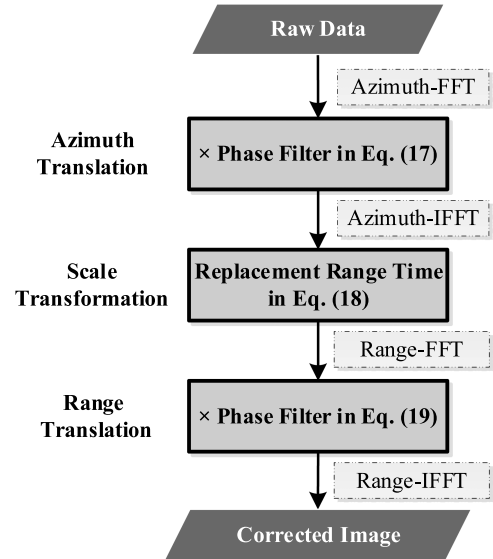


Fig. 5. Flowchart of image correction.

parallelogram. The following processing steps will correct such distortion effect.

First, from the geometric relationships, the angle of deformation can be obtained in

$$\tan \theta_g = \frac{l_2 \sin \theta_d}{\sqrt{(y_0 + l_2)^2 + H^2} - R_0} \quad (16)$$

where θ_d is the squint angle.

As shown in Fig. 5, in Step 1, the original SAR image is first transformed from azimuth time domain η to the azimuth frequency domain f_d , i.e., $S_r(t, \eta) \rightarrow S_r(t, f_d)$.

In Step 2, we transform parallelogram to rectangle by multiplying a phase factor as

$$S_r^{\text{GC}}(t, f_d) = S_r(t, f_d) \exp\left(j2\pi f_d \frac{l_2 \tan \theta_d}{v}\right) \quad (17)$$

where f_d indicates the Doppler center and v is the speed of the platform.

Subsequently, it is transformed back to the azimuth time domain $S_r^{\text{GC}}(t, \eta)$, and a scaling factor of t is applied, i.e.

$$t' = \frac{\tan \theta_g}{\tan \theta_d} t. \quad (18)$$

Now we have corrected the parallelogram A'B'C'D' to the rectangle with the same size of ABCD. Next, we need to compensate the shift in range dimension. First, transform $S_r^{\text{GC}}(t', \eta)$ to the range frequency domain $S_r^{\text{GC}}(f', \eta)$ and then multiply a phase factor as follows:

$$S_r^{\text{GC}}(f', \eta) = S_r^{\text{GC}}(f', \eta) \exp\left(j2\pi f' \frac{2(R_0/\cos \theta_d - R_0)}{c}\right). \quad (19)$$

Finally, transform $S_r^{\text{GC}}(f', \eta)$ back to the range time domain and it will restore the undistorted image.

If one wants to further perform geocoding, at least three reference corner reflectors or a landmark building with known

TABLE I
RADAR PARAMETER IN SIMULATION

Symbol	Parameters	Values
f_c	carrier frequency	15.2GHz
B	frequency bandwidth	2.5GHz
H	platform altitude	300m
PRF	Pulse repetition frequency	2000Hz
θ_a	azimuth beam width	6°
θ_r	range beam width	10°
θ_{in}	incident angle	65°
v	platform velocity	10m/s
F_s	sampling rate	25MHz
ρ_a	Azimuth Resolution	9.42cm
ρ_r	Range Resolution	6cm
S	Width of Swath	691.17m
L_{sar}	Synthetic Aperture Length	123.89m
R_{ref}	Reference Range	709.86m

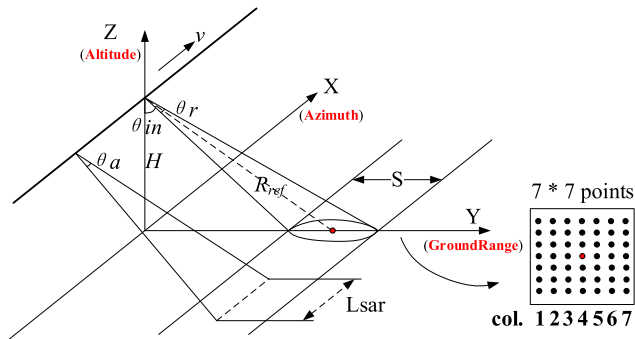


Fig. 6. Imaging geometry of the simulation case where a 7×7 point target grid is in the scene center. Simulation parameters are listed in Table I.

latitude and longitude coordinates should be included in the image. Additionally, these reference coordinates can be used to estimate the latitude and longitude coordinates of the platform trajectory.

IV. SIMULATION ANALYSES

In this section, raw signals are simulated using the parameters shown in Table I to validate the SLAI algorithm. It employs the FMCW mode and observes a 7×7 grid point targets with a horizontal and vertical spacing of 25 m. The simulated scene is shown in Fig. 6. The platform flies from -200 m to $+200$ m along the X -axis. The simulation uses the actual platform trajectory measured by GPS/INS in an experiment of the FUSAR-Ku, so the trajectory contains realistic position error and attitude error, but the vibration error cannot be completely restored due to the low sampling rate of GPS/INS. The data of platform position and attitude are shown in Fig. 7(a) and (b), respectively. The pitch angle and roll angle of the multirotor will change in stages due to its maneuvering features and the SWaP of platform. The accumulation angular variation range is greater than 6° , where the center direction of the beam is rotated, resulting in a coupling phase that cannot be ignored.

The SAI algorithm is used to focus the simulated echo data. First, the entire original data is divided into six overlapping segments along the azimuth direction. The total length of the azimuth dimension of the simulated data is 398.894 m, and

the lattice target covers the range of -80 – 80 m in the azimuth direction, of which segments 3, 4, and 5 contain the complete target area. The lengths of each section are 160.51, 123.89, and 267.67 m, respectively. The squint angles were 8.4° , -2.1° , and 3.2° , respectively. One of the imaging results of a segment is shown in Fig. 7(c). Then, motion compensation and imaging are performed on each segment separately. Finally, the final imaging results of each segment are stitched to obtain the entire image, as shown in Fig. 7(d).

The segment imaging results have incomplete apertures on both sides, so the focusing results of the point target will have azimuthal broadening. The mainlobe 3 dB width of azimuth point spread function (PSF) is 14.11 cm. The peak side lobe ratio (PSLR) is about 10.28 dB. The resolution is the same everywhere in the final imaging range. The 3 dB mainlobe width of azimuth PSF is 9.46 cm, which is close to the theoretical value of 9.42 cm. Slight degradation might be caused by segment stitching, and the resolution loss is less than $\lambda/4$. It will not affect the coherent processing of SAR images. The PSLR is about 13.25 dB, close to the theoretical value.

In the simulation, we take GPS/INS as the true value of the platform motion trajectory. According to simulated data, we can calculate the phase variation range during the entire flight process. After removing the constant phase of the reference slant range, the reference phase curve is shown by the blue line in Fig. 7(e). The reference phase variation range is from -40 to 80 rad. Although the overall shape is approximately a second-order curve, the high-order phase term is obviously superimposed, and the curve is asymmetrical, which means the azimuth Doppler center is not zero.

The final phase history estimated by the SAI algorithm is shown as the red line in Fig. 7(e). The SAI algorithm adopts a local linear substitution method, such as the enlarged part in the green box. The estimation accuracy of the complete phase history estimated and the reference phase history is less than 2 rad.

According to the estimated parameters of each segment, the trajectory of each segment is calculated according to (12). The trajectory coordinates are in the XYZ coordinate system, where the X -axis represents the azimuth dimension, the Y -axis represents the ground range dimension, which is the projected component of the slant range on the ground, and the Z -axis represents the altitude dimension.

We further stitch the estimated trajectories of each segment. During the imaging process of the SAI algorithm, multiple subimages like Fig. 7(c) will be generated. First, 3–4 strong points are extracted in the intersection area of segments, such as the point in red box in Fig. 7(c). Using the subaperture spectrum and the correlation of the phase-Doppler curve, the transformation matrix is calculated. Finally, the segment $q + 1$ of trajectories are transformed to segment $q + 1$, and stitching in turn to obtain the final complete trajectory, as shown in Fig. 7(a).

The trajectory estimation error is shown in Fig. 7(f), which shows that we can achieve centimeter-level accuracy in azimuth dimension (X -axis) and ground range dimension (Y -axis), and decimeter-level accuracy in height dimension (Z -axis). Because the SAR image is a 2-D image, and there is overlapping in

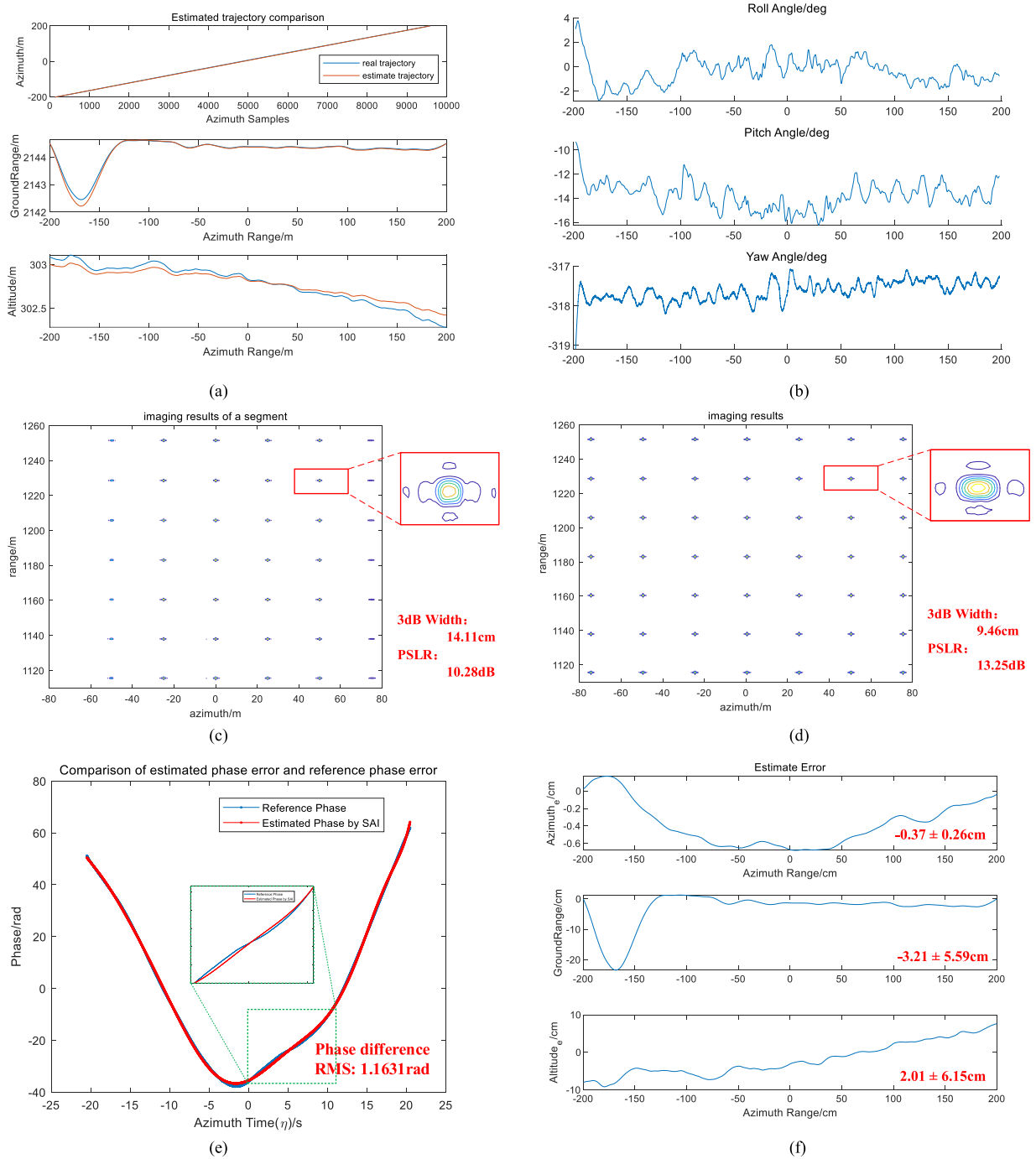


Fig. 7. Point target imaging simulation results. (a) Comparison result of the estimated trajectory (red line) and the reference trajectory (blue line) in the coordinate system in Fig. 6, which are in azimuth direction (X -axis), ground range direction (Y -axis), and altitude direction (Z -axis). (b) Measured GPS/INS attitude angle data, including roll angle, pitch angle, and yaw angle. (c) Imaging results of a segment, and the mainlobe 3 dB width and PSRL of a focused point are 14.11 cm, 10.28 dB, respectively. (d) Final imaging results after stitching segments, and the mainlobe 3 dB width and PSRL of a focused point are 9.46 cm, 13.25 dB, respectively. (e) Estimated phase and reference phase comparison curve. The root mean square (RMS) of the error between the two is 1.1631 rad. (f) Trajectory estimation error in three-dimension (Note that the statistical errors are denoted in each panel in the form of “mean \pm std”).

the measurement process, the estimation error of the altitude dimension exceeds that of other dimensions. The estimation accuracy of the azimuth dimension (X -axis) and ground range dimension (Y -axis) is positively related to the PRF and bandwidth. When the azimuth interval is less than $\lambda/4$, its estimation

accuracy can reach $\lambda/10$. Since multiple pulses, which contain the reference strong scatterers, are highly correlated after compensating for the Doppler shift, the azimuth estimation has high accuracy. On the slant range dimension, we can only rely on the signal chirp. Therefore, the estimation accuracy of the

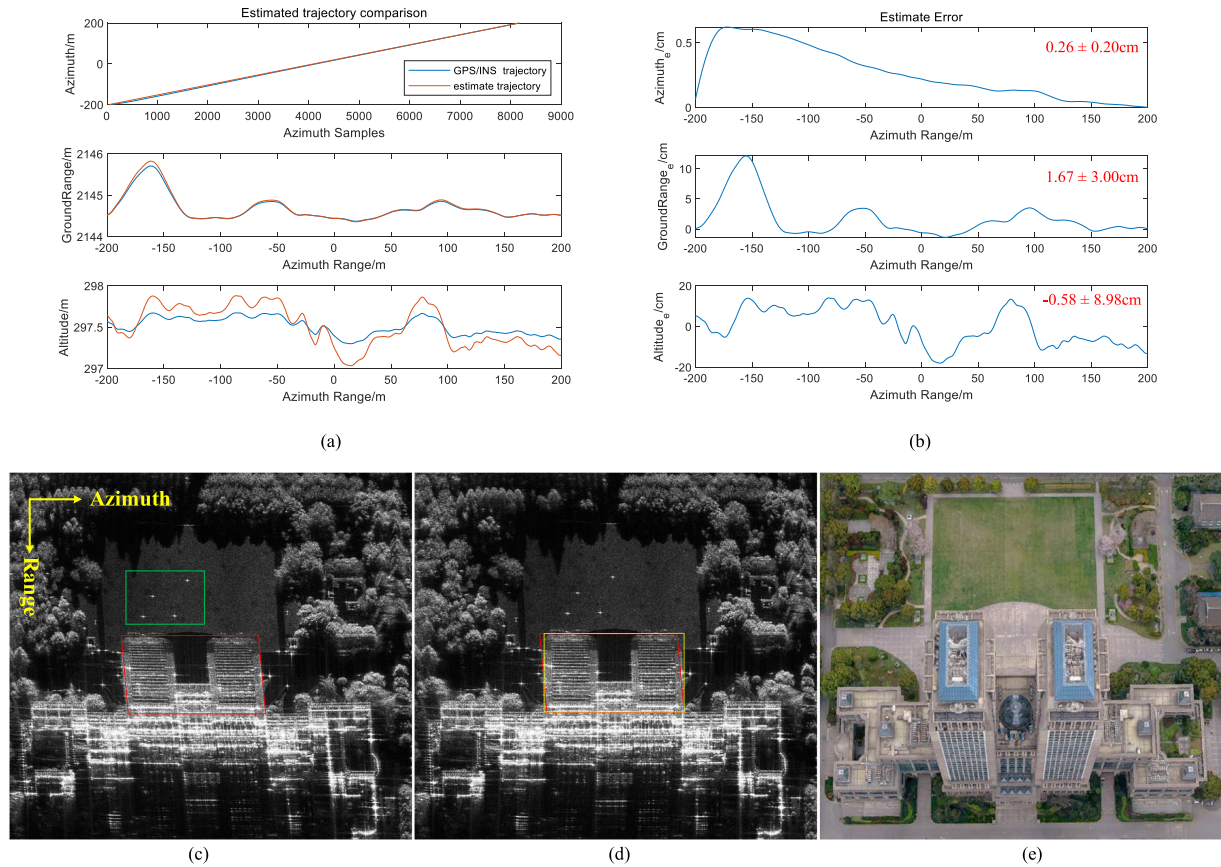


Fig. 8. FUSAR-Ku system flight experiment results. (a) Comparison results of estimated trajectory and GNSS/INS trajectory of FUSAR-Ku experiment in azimuth dimension (X -axis), ground range dimension (Y -axis), altitude dimension (Z -axis). (b) Errors of estimated trajectory and GNSS/INS trajectory in azimuth dimension (X -axis), ground range dimension (Y -axis), altitude dimension (Z -axis) (Note that the statistical errors are denoted in each panel in the form of “mean \pm std”). (c) Focusing effect of Guanghua tower, Handan Campus of Fudan University. The imaging result is deformed due to the rotation of the platform, such as the building in the red box, the two sides should be perpendicular to each other. (d) Image of Guanghua tower after geometric correction. The correction from the red box to the yellow box is shown. (e) 3-D model of Guanghua tower for comparison.

ground range dimension is basically in the same order as the range resolution.

V. EXPERIMENTAL RESULTS

From 2020 to 2021, we have conducted a number of flight experiments with the FUSAR-Ku system to verify the SLAI algorithm. The experiments were carried out on the Handan and Jiangwan campuses of Fudan University. We designed multiple parallel trajectories across the campus. During the flight, we encountered sunny and moderate rain. Ground winds are between level 3 to 6. The algorithm works robustly in these environments. The altitude of platform is about 450 m, and the swath is about 1400 m. Reference slant range is 912 m. The platform speed is 10–15 m/s. The system setup was shown in Fig. 2. Other parameters are shown in Table I.

In the experimental preparation stage, four corner reflectors were placed on the ground. We plan to use it as a calibrator for the geometric correction as described in Section III-C, and also use it for radiometric and polarimetric calibration. The ground station uses RTK antenna to communicate with the UAV, and displays the flight status of the multirotor in real time.

The results of imaging and trajectory estimation using the SLAI algorithm are shown in Fig. 8. It shows estimated trajectories and imaging results in azimuth dimensions from -200 to 200 m. From the results of trajectory estimation, it can be seen that the platform is intermittently affected by wind, which leads to large fluctuations along the trajectory ($> 10\lambda$). In Fig. 8(a), the reconstructed trajectories are compared in three dimensions relative to the GPS/INS measurements. The estimation errors are shown and evaluated in Fig. 8(b). The experimental trajectory estimation results are basically consistent with the simulation results. The errors of the azimuth dimension (X -axis), ground range dimension (Y -axis), and altitude dimension (Z -axis) are centimeter-level, centimeter-level, and decimeter-level, respectively. Note that the actual positioning error should be better as this is the sum of both the GPS/INS measurement error and the SLAI error.

By accurately reconstructing the trajectory of platform, we can also use the relative position between the platform and reference targets in the illuminated scene to geometrically correct the image. Take the imaging result of Guanghua Tower as an example, as shown in Fig. 8(c), the edge of the building is annotated by a red box, and it can be seen that the red box is a parallelogram,



Fig. 9. Geocoding results of the Handan campus, as well as SLAI imaging results and optical images of typical buildings.

which should appear as a rectangle. For geometric correction, four corner reflectors were used as reference targets. During the experimental preparation stage, their latitude and longitude were recorded and the estimated trajectories can be converted into the WGS84 geographic coordinate system. After correction by the method in Section III-C, the results shown in Fig. 8(d) are obtained. Apparently, the shape of the building after correction denoted by yellow box appears to be correct. The optical photo of Guanghua Tower is shown in Fig. 8(e) as a reference. The imaging effect of the point target is illustrated by the focusing effect of four corner reflectors. Their 3 dB mainlobe width is about 9.53–9.98 cm, PSLR is between 13.01 and 13.27 dB, and entropy is between 0.31 and 0.67.

According to the ratio of the peak value of the reference target to the theoretical value in the image, the image is radiometrically corrected to calibrate the dynamic range of the image. Then, according to the theoretical corner reflector scattering matrix, the Quegan algorithm is used to perform polarization calibration on the image. The imaging results of the quad-polarization channels (HH/HV/VH/VV) are decomposed, and the difference channel, the cross channel, and the sum channel are used to form an RGB pseudocolor image. As shown in Fig. 9, the color distributions of the pseudocolor images of the

Gymnasium and Science Building are consistent with the scattering properties of the target. Buildings parallel to the flight trajectory are equivalent to the dihedral angle of the vertical incidence of electromagnetic waves, and the co-polarization channels are stronger, which is red in the pseudocolor image. Plants such as sycamore trees are mainly multiple scattering components, and thus the cross-polarization channels are strong, which is green in the pseudocolor image.

Finally, the slant range-azimuth image can be projected to the ground range-azimuth image, and the affine matrix of the SAR image can be calculated according to the geographic coordinates of the estimated trajectory, and the image can be geocoded. As shown in Fig. 9, it is the complete SAR image of the Handan campus, and the upper right corner is the campus image captured by camera on a drone. The comparison of optical images and SAR images of typical buildings is shown in Fig. 9.

VI. CONCLUSION

This study proposes the novel SLAI algorithm specifically for MiniSAR onboard small platforms such as multirotors. It achieves SAR imaging without auxiliary positioning such as

GNSS/INS. In addition, it can simultaneously estimate accurate position of the platform while performing SAR imaging. Thus, it realizes SLAI on multirotor with radar sensor only. Experimental results with the FUSAR-Ku system demonstrate superior performance of the SLAI algorithm, i.e., 0.1 m-resolution imaging is achieved with the Ku-band radar with simultaneously centimeter-to-decimeter level of positioning accuracy. The resolution and accuracy of the final image are demonstrated, and the phase estimation error is less than 2 rad.

The current implementation of SLAI takes advantage of parallel processing. It has the possibility of being improved into real-time processing. For example, the sequential processing step of segment stitching can be further parallelized in a recursive fashion. There are additional works for full processing of the FUSAR-Ku system. For example, this system is designed as a polarimetric SAR interferometry (PolInSAR) system with two dual-pol antennas. It is also necessary to continue to study the coherent processing between range/azimuth multichannels. The multirotor-borne MiniSAR will open a wide range of applications in surveying, monitoring, disaster relief, and defense areas.

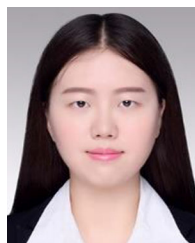
ACKNOWLEDGMENT

The authors would like to acknowledge the helps provided by Zhongke Yuda and Henan Zhongzhicheng Technology Company during the FUSAR-Ku experiments.

REFERENCES

- [1] Y. Luomei and F. Xu, "Motion compensation for multirotors minisar system," in *Proc. IEEE Int. Geosci. Remote Sens. Symp.*, 2021, pp. 5143–5146, doi: [10.1109/IGARSS47720.2021.9553707](https://doi.org/10.1109/IGARSS47720.2021.9553707).
- [2] A. Bhardwaj et al., "UAVs as remote sensing platform in glaciology: Present applications and future prospects," *Remote Sens. Environ.*, vol. 175, pp. 196–204, 2016, doi: [10.1016/j.rse.2015.12.029](https://doi.org/10.1016/j.rse.2015.12.029).
- [3] G. Virone et al., "Antenna pattern verification system based on a micro unmanned aerial vehicle (UAV)," *IEEE Antennas Wireless Propag. Lett.*, vol. 13, pp. 169–172, 2014.
- [4] G. Wang et al., "Robust two-dimensional spatial-variant map-drift algorithm for UAV SAR autofocus," *Remote Sens.*, vol. 11, no. 3, 2019, Art. no. 340, doi: [10.3390/rs11030340](https://doi.org/10.3390/rs11030340).
- [5] M. Ding, X. Liang, L. Tang, Z. Wen, X. Wang, and Y. Wang, "Micro FMCW SAR with high resolution for mini UAV," in *Proc. Int. Conf. Microw. Millimeter Wave Technol.*, 2018, pp. 1–3, doi: [10.1109/ICMMT.2018.8563465](https://doi.org/10.1109/ICMMT.2018.8563465).
- [6] S. Stanko, W. Johannes, R. Sommer, A. Wahlen, M. Schröder, and M. Caris, "SUMATRA - A UAV based miniaturized SAR system," in *Proc. 9th Eur. Conf. Synthetic Aperture Radar*, 2012, pp. 437–440.
- [7] W. Johannes et al., "Implementation of a 35 GHz SAR sensor and a high resolution camera to enable real-time observation," in *Proc. 10th Eur. Conf. Synthetic Aperture Radar*, 2014, pp. 1–4.
- [8] Y.-L. Li, X.-D. Liang, L.-J. Zhou, L.-Y. Chen, Y.-W. Dong, and C.-B. Ding, "Introduction to IECAS-SAR — A multi-frequency polarimetric airborne SAR," in *Proc. IEEE Geosci. Remote Sens. Symp.*, 2014, pp. 1085–1088, doi: [10.1109/igarss.2014.6946617](https://doi.org/10.1109/igarss.2014.6946617).
- [9] Y. Zhang, D. Zhu, X. Mao, X. Yu, J. Zhang, and Y. Li, "Multirotor video synthetic aperture radar: System development and signal processing," *IEEE Aerosp. Electron. Syst. Mag.*, vol. 35, no. 12, pp. 32–43, Dec. 2020.
- [10] M. Y. Chua et al., "The maiden flight of hinotori-C: The first C band full polarimetric circularly polarized synthetic aperture radar in the world," *IEEE Aerosp. Electron. Syst. Mag.*, vol. 34, no. 2, pp. 24–35, Feb. 2019.
- [11] O. Frey, C. Magnard, M. Rüegg, and E. Meier, "Focusing of airborne synthetic aperture radar data from highly nonlinear flight tracks," *IEEE Trans. Geosci. Remote Sens.*, vol. 47, no. 6, pp. 1844–1858, Jun. 2009.
- [12] J. J. M. de Wit, A. Meta, and P. Hoogeboom, "Modified range-Doppler processing for FM-CW synthetic aperture radar," *IEEE Geosci. Remote Sens. Lett.*, vol. 3, no. 1, pp. 83–87, Jan. 2006.

- [13] D. G. Thompson, A. E. Robertson, D. V. Arnold, and D. G. Long, "YINSAR: A compact, low-cost interferometric synthetic aperture radar," in *Proc. IEEE Radar Conf. Radar Next Millennium*, 1999, pp. 221–226.
- [14] E. Zaugg, D. Hudson, and D. Long, "The BYU SAR: A small, student-built SAR for UAV operation," in *Proc. IEEE Int. Symp. Geosci. Remote Sens.*, 2006, pp. 411–414.
- [15] J. J. M. de Wit and P. Hoogeboom, "High resolution FM-CW SAR performance analysis," in *Proc. IEEE Int. Geosci. Remote Sens. Symp. Proc.*, vol. 7, 2003, pp. a4317–a4319.
- [16] D. G. Long, E. Zaugg, M. Edwards, and J. Maslanik, "The microasar experiment on CASIE-09," in *Proc. IEEE Int. Geosci. Remote Sens. Symp.*, 2010, pp. 3466–3469.
- [17] D. Henke et al., "Miranda35 experiments in preparation for small UAV-based SAR," in *Proc. IEEE Int. Geosci. Remote Sens. Symp.*, 2019, pp. 8542–8545, doi: [10.1109/IGARSS.2019.8897902](https://doi.org/10.1109/IGARSS.2019.8897902).
- [18] M. Ding, L. Tang, L. Zhou, X. Wang, Z. Weng, and J. Qu, "W band Mini-SAR on multi rotor UAV platform," in *Proc. IEEE 2nd Int. Conf. Electron. Inf. Commun. Technol.*, 2019, pp. 416–418, doi: [10.1109/ICE-ICT.2019.8846356](https://doi.org/10.1109/ICE-ICT.2019.8846356).
- [19] R. Yang et al., *High-Resolution Microwave Imaging*. Singapore: Springer, 2018.
- [20] A. Evers and J. A. Jackson, "A generalized phase gradient autofocus algorithm," *IEEE Trans. Comput. Imag.*, vol. 5, no. 4, pp. 606–619, Dec. 2019.
- [21] Y. Li and S. O'Young, "Kalman filter disciplined phase gradient autofocus for stripmap SAR," *IEEE Trans. Geosci. Remote Sens.*, vol. 58, no. 9, pp. 6298–6308, Sep. 2020.
- [22] T. Xiong, M. Xing, Y. Wang, S. Wang, J. Sheng, and L. Guo, "Minimum-entropy-based autofocus algorithm for SAR data using chebyshev approximation and method of series reversion, and its implementation in a data processor," *IEEE Trans. Geosci. Remote Sens.*, vol. 52, no. 3, pp. 1719–1728, Mar. 2014.
- [23] J. Chen, M. Xing, H. Yu, B. Liang, J. Peng, and G.-C. Sun, "Motion compensation/autofocus in airborne synthetic aperture radar: A review," *IEEE Geosci. Remote Sens. Mag.*, vol. 10, no. 1, pp. 185–206, Mar. 2022.
- [24] M. Bao, S. Zhou, L. Yang, M. Xing, and L. Zhao, "Data-driven motion compensation for airborne bistatic SAR imagery under fast factorized back projection framework," *IEEE J. Sel. Topics Appl. Earth Observ. Remote Sens.*, vol. 14, pp. 1728–1740, Jun. 2020.
- [25] Y. Zhang, D. Zhu, X. Mao, G. Zhang, and H. Leung, "Multirotor UAV-borne repeat-pass CSM-VideoSAR," *IEEE Trans. Aerosp. Electron. Syst.*, vol. 58, no. 3, pp. 2601–2605, Jun. 2022.
- [26] Y. Luomei and F. Xu, "Segmental aperture imaging algorithm for multirotor UAV-borne MiniSAR," *IEEE Trans. Geosci. Remote Sens.*, to be published, doi: [10.1109/JSTARS.2022.3190940](https://doi.org/10.1109/JSTARS.2022.3190940).
- [27] K. T. J. Klein, F. Uysal, M. C. Cuenca, M. P. G. Otten, and J. J. M. de Wit, "Radar-aided navigation system for small drones in GPS-denied environments," in *Proc. IEEE Radar Conf.*, 2021, pp. 1–6, doi: [10.1109/RadarConf2147009.2021.9455317](https://doi.org/10.1109/RadarConf2147009.2021.9455317).
- [28] K. T. J. Klein, F. Uysal, M. C. Cuenca, M. P. G. Otten, and J. J. M. de Wit, "Pulse-to-pulse radar-aided positioning using multibeam autofocus," in *Proc. 18th Eur. Radar Conf.*, 2022, pp. 257–260, doi: [10.23919/EURAD50154.2022.9784580](https://doi.org/10.23919/EURAD50154.2022.9784580).



Yixiang Luomei (Student Member, IEEE) received the B.E. and M.E. degrees in electronic and communication engineering from Xidian University, Xi'an, China, in 2014 and 2018, respectively. She is currently working toward the Ph.D. degree in electronics and information with the School of Information Science and Technology, Fudan University, Shanghai, China. Her research interests include MIMO radar signal processing and UAV SAR imaging.



Feng Xu (Senior Member, IEEE) received the B.E. (Hons.) degree in information engineering from Southeast University, Nanjing, China, in 2003, and the Ph.D. (Hons.) degree in electronic engineering from Fudan University, Shanghai, China, in 2008.

From 2008 to 2010, he was a Postdoctoral Fellow with the NOAA Center for Satellite Application and Research (STAR), Camp Springs, MD, USA. From 2010 to 2013, he was a Research Scientist with Intelligent Automation Inc., Rockville, MD. Since 2013, he has been a Professor with the School of Information

Science and Technology. He currently serves as a Vice Dean of the School of Information Science and Technology and the Director of the MoE Key Lab for Information Science of Electromagnetic Waves. He has published more than 60 papers in peer-reviewed journals and coauthored 3 books, among many conference papers and patents. His current research interests include electromagnetic scattering theory, SAR information retrieval, and advanced radar systems.

Dr. Xu was the recipient of the second-class National Nature Science Award of China in 2011, the 2014 recipient of the Early Career Award of IEEE Geoscience and Remote Sensing Society, and the 2007 recipient of the SUMMA graduate fellowship in the advanced electromagnetics area. He currently serves as the Associate Editor for IEEE GEOSCIENCE AND REMOTE SENSING LETTERS. He is the founding Chair of IEEE GRSS Shanghai Chapter.



Yongwei Dong (Member, IEEE) received the B.E. (Hons.) degree in signal and information processing from the University of Science and Technology of China, Hefei, China, and the Ph.D. (Hons.) degree in signal and information processing from the Institute of Electronics, Chinese Academy of Sciences, Beijing, China, in 2002 and 2007, respectively.

From 2007 to 2014, he was an Assistant Researcher with the Institute of Electronics, Chinese Academy of Sciences. From 2014 to 2016, he was a Vice Researcher with the Institute of Electronics, Chinese

Academy of Sciences. Since 2016, he has served as the Vice Director of the State Key Laboratory of Microwave Radiation. He currently serves as the legal Representative of Zhongke Yuda (Beijing) Technology Co., Ltd., Beijing. He has published more than 20 papers in peer-reviewed journals, among many conference papers and patents. His current research interests include micro-RADAR design, real-time signal processing, and low, small and slow target detection.



Feng Wang (Member, IEEE) received the B.S. and M.S. degrees in remote sensing from Information Engineering University, Zhengzhou, China, in 2006 and 2010, respectively, and the Ph.D. degree in electronic engineering from Fudan University, Shanghai, China, in 2017.

He was a Visiting Scholar with the Technical University of Munich, Germany, in 2013, and a Postdoctoral Research Fellow with the State Key Laboratory of Lunar and Planetary Sciences, Macau University of Science and Technology, Macau, China, from 2017

to 2018. He was with the Shanghai Institute of Technical Physics, Chinese Academy of Sciences, Shanghai, as an Assistant Research Fellow. He is currently an Assistant Professor with the Key Laboratory for Information Science of Electromagnetic Waves (Ministry of Education), School of Information Science and Technology, Fudan University. His research interests include SAR/ISAR imaging, target recognition and UAV borne remote sensing.